JOURNAL OF PROPULSION AND POWER
Vol. 12, No. 6, November–December 1996

Effects of Nozzle Geometry on Parallel Injection into a Supersonic Flow

Diana D. Glawe* and Mo Samimy†
Ohio State University, Columbus, Ohio 43210
Abdollah S. Nejad‡
U.S. Air Force Wright Laboratory, Wright–Patterson Air Force Base, Ohio 45433-6563
and
Tzong H. Chen§
Taitech, Inc., Beavercreek, Ohio 45440-3568

Fuel injection from the base of a two-dimensional extended strut bounded above and below by nominal Mach 2 freestreams was investigated. Without injection, a two-dimensional wake flow exists behind the base of the strut. When fuel, simulated with helium, is injected parallel to the nominal Mach 2 freestreams, a highly three-dimensional complex flowfield results. The behavior of the flowfield generated by a circular injection nozzle was compared to the results obtained using two asymmetric nozzle geometries: 1) an elliptic nozzle and 2) a circular nozzle with vortex-generating tabs. The results show that the injected fuel jets are confined to the wake region downstream of the strut; thus the spread of the jets in the transverse direction is highly limited. The jet emanating from the circular nozzle with two tabs oriented normal to the span of the extended strut exhibited the best mixing. The second best mixing was exhibited by the elliptic nozzle, with its major axis normal to the span of the extended strut.

Nomenclature

d = nozzle exit diameter
h = strut thickness or step height
M = Mach number
P = static pressure
$\ddot{P}$ = momentum flux
P_0 = stagnation pressure
T = static temperature
T_0 = stagnation temperature
U = streamwise velocity
ρ = density
Ψ = ratio of calculated static pressure of the jet at nozzle exit to the static pressure of freestream air

Introduction

GASEOUS injection into supersonic flows has many engineering applications. One application of primary interest to the aerospace community is the injection of gaseous hydrogen or hydrocarbon fuels in supersonic combustion ramjet (scramjet) engines. It has been argued that air-breathing supersonic combustion engines offer the best performance for a single-stage-to-orbit flight vehicle.[1] However, the challenges involved in realizing such a vehicle are daunting. These challenges include designing an injection scheme to produce optimal fuel–air mixing and combustion within the space and time constraints of a supersonic combustor.

Fuel–air mixing in supersonic flows suffers from very short time scales and inherently low mixing rates at higher Mach numbers.[2,3] Parallel, normal, and oblique injection schemes have all been investigated. Normal injection produces the best mixing, but a greater total pressure loss primarily because of the generation of a strong bow shock.[4] Injection at oblique angles to the flow has shown an improved total pressure recovery relative to normal injection and an improved mixing and fuel distribution relative to parallel injection.[5] Parallel injection of fuel can provide a significant component of the engine thrust at high flight Mach numbers, but typically provides limited mixing capability. Passive mixing enhancement has been explored through the use of nozzle geometry[6–8] and shock impingement.[9,10]

Fuel penetration and distribution are of major concern in the design of injectors for supersonic combustors. To date, some of the practical injector designs employ in-flow struts for even fuel placement and distribution within the combustor flowfield. To enhance mixing associated with parallel injection, several investigators have employed discrete ramp injectors designed to enhance mixing by vortex shedding, flow separation, and shock impingement.[10] An advantageous consequence of injection from ramps and struts is the formation of a recirculation zone. In combustion applications, the recirculation zone enables back mixing of partially or wholly burned gases into the fuel–air mixture, thereby sustaining self-ignition (i.e., flame holding). Although there have been several studies of two-dimensional flow behind a strut,[11–13] experimental data are unavailable for injection from the base of a two-dimensional strut with supersonic flow. The objectives of this investigation were to determine the fundamental characteristics of parallel fuel injection into a supersonic freestream from the base of an extended strut and to explore passive mixing enhancement through the use of different injector nozzle geometries.

Facility

The present research was conducted in the supersonic combustion research facility at the Aero Propulsion and Power Directorate at Wright Laboratory.[14] Various turbine and reciprocating compressors are available to produce a continuous flow of approximately 15.5 kg/s of clean, compressed air at a maximum supply pressure of 5 MPa. Half of this air can be heated to a maximum stagnation temperature of 920 K using

Received Jan. 15, 1996; revision received April 25, 1996; accepted for publication April 29, 1996.

*Research Engineer, Department of Mechanical Engineering. Member AIAA.
†Professor, Department of Mechanical Engineering. Associate Fellow AIAA.
‡Senior Research Engineer, Advanced Propulsion Division, Experimental Research Branch. Member AIAA.
§Senior Research Scientist. Senior Member AIAA.

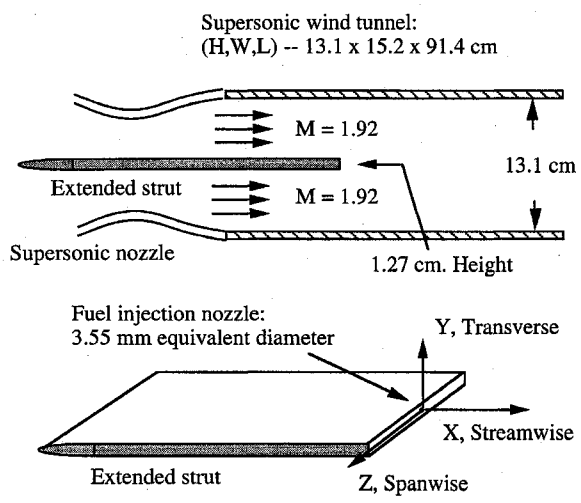

Fig. 1 Schematic of extended strut and reference coordinate system.

a gas-fired heat exchanger. The nozzle section is composed of two identical planar two-dimensional nozzles, one on either side of the strut, that produce the desired expansion to a nominal Mach number of 2.0 at the entrance to the test section (Fig. 1).

The constant-area test section is 15.2 cm wide by 13.1 cm high. A pair of fused silica windows mounted in the side walls and a single fused silica window mounted in the top wall provide the desired optical access. The side windows allow direct viewing of the entire transverse dimension of the test section and approximately 44 cm in the streamwise dimension. The top window provides the same access length in the streamwise dimension with approximately 7 cm along the spanwise dimension.

For the present experiments, a 1.27-cm-thick strut (held in place by grooves in the tunnel side walls) provided rigid support for the injector nozzles and had the added benefit of producing a recirculation zone for flame holding in combustion applications. The 94-cm-long strut extended 7 cm into the settling chamber and downstream a distance of approximately 7 cm into the test section. This strut is similar to a typical splitter plate used in shear-layer studies[2,3,15] with the following exceptions: the flow velocity is identical on both sides of the strut and the base of the strut is blunt rather than tapered to a knife edge. By extending the strut upstream through the nozzle into the settling chamber, as shown in Fig. 1, and using the method of characteristics to design the nominal Mach 2 nozzles, the presence of strong waves in the approaching freestreams was avoided. Laser Doppler velocimetry (LDV) mean velocity profiles show very repeatable, symmetric, and uniform Mach 1.92 flow above and below the strut with turbulence intensities less than 1% in the freestream.[16]

The injection nozzles were rigidly mounted in the base of the strut at the centerline of the wind tunnel and were held in place by a retaining plate. The modular design of the nozzles and retaining plate allowed quick changeover of the interchangeable nozzles and the nozzle orientations. Injection from circular, circular-with-tabs, and elliptic nozzles was investigated in this study. Photographs of the nozzle tips are shown in Fig. 2. All three nozzles were machined by electric discharge machining (EDM) to converge to a minimum cross-sectional area of 9.9 mm^2 at the nozzle exit.

The diameter of the circular and circular-with-tabs nozzles was 3.55 mm. The circular-with-tabs nozzle included two tabs located on opposite sides of the nozzle exit circumference. The tab width was 0.86 mm, 24% of the nozzle exit diameter. The tabs extended into the flow a projected length of 0.38 mm, 11% of the nozzle exit diameter. Experiments have shown that a delta tab, which creates a projected blockage in the shape of a triangle with the apex of the triangle directed into the jet flow, is the optimal shape for streamwise vortex generation.[17] Furthermore, the tabs would ideally be infinitely thin to maximize the vortex-inducing pressure gradient across them. However, machining and strength limitations require thicker tabs, with a rectangular shape. The tabs were angled downstream into the jet flow with an angle of 135 deg from the nozzle wall, the angle shown to have the greatest mixing effect.[17]

The elliptic nozzle had a semimajor axis of 6.15 mm and a semiminor axis of 2.05 mm, resulting in an AR of 3:1 and an equivalent diameter of 3.55 mm for a circular nozzle of the same cross-sectional area. A 3:1 AR elliptic nozzle has been shown to exhibit the maximum spread for injection into a coaxial flow[18] and falls in the range of ARs examined in previous freejet studies.[19] The elliptic shape was chosen over other simple geometries known to increase mixing, such as triangular or rectangular, because corners at the nozzle exit induce vortices and produce a more complex flow.[6] Furthermore, the elliptic nozzle represents oblong nozzles, which undergo distinct axis-switching, a mechanism shown to be a key factor in increased mixing as compared to circular jets.[19] The circular-with-tabs nozzle was chosen because of its recognized mixing enhancement capability.[7,8,17] In additional support of the selection of the elliptic and tabbed nozzles, similar nozzle geome-

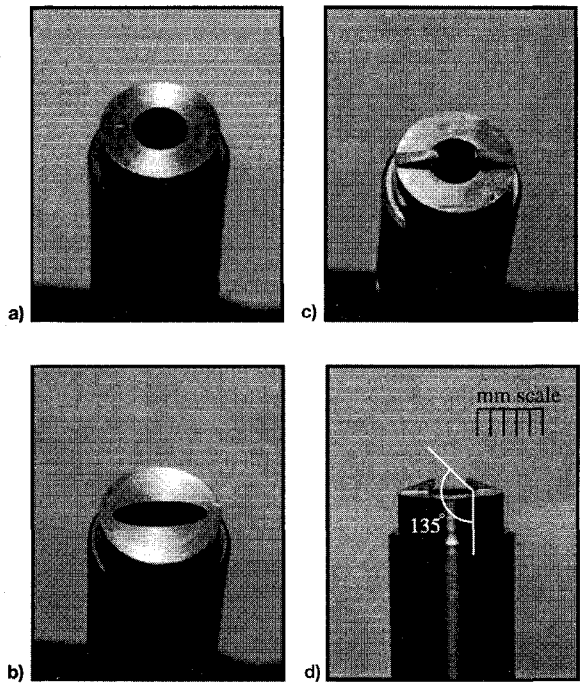

Fig. 2 Photographs of the tips of the injector nozzles: a) circular, b) elliptical, and c) and d) circular-with-tabs.

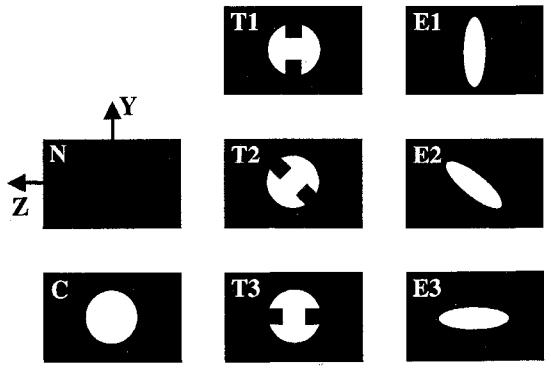

Fig. 3 Schematic of nozzle orientations. No-injection (N) case and injection cases: circular (C), circular-with-tabs (T1, T2, T3), and elliptic (E1, E2, E3).

Table 1 Operating conditions for helium injection into Mach 1.92 air freestream

Flow/conditions	P_0, kPa	T_0, K	M	P, kPa	T, K	ρ, kg/m^3	U, m/s	$\ddot{P}$, Pa
Freestream	345	300	1.92	50	172	1.01	506	2.58×10^5
Helium[a] ($\Psi = 1$)	97	300	1	47	225	0.10	871	0.78×10^5
Helium[a] ($\Psi = 2$)	207	300	1	101	225	0.22	871	1.72×10^5
Helium[a] ($\Psi = 4$)	414	300	1	201	225	0.44	871	3.44×10^5

[a]Helium conditions at exit plane of jet nozzle.

tries were considered to be the most promising candidates for future research in studies of injection through different nozzles at the base of a swept ramp.[20]

The circular nozzle was chosen as the reference nozzle for comparison. The elliptic and circular-with-tabs nozzles were rotated to examine the effects of different angular orientations. Injection from the nozzles with the orientations shown in Fig. 3 will hereafter be referred to by the symbols C, T1, T2, T3, E1, E2, and E3. The no injection case will be denoted as N.

Helium was used as the injectant to simulate hydrogen fuel. The helium mass flow rate was varied so that the ratio of the static pressure of the helium jet at the nozzle exit to the static pressure of the freestream air was approximately $\Psi = P_{\text{nozzle}}/P_{\text{freestream}} = 1$, 2, and 4. The $\Psi = 4$ static pressure ratio was chosen to obtain a highly underexpanded jet and was the focus of this study because it most accurately mimics the operational fuel injection conditions in scramjet propulsion systems. The injectant velocity at the exit of the converging nozzles was sonic in all cases. A pressure transducer mounted in the helium flow line just outside the tunnel wall recorded the instantaneous helium stagnation pressure. The stagnation temperature of the helium was equal to ambient temperature. The static pressure of the helium jet at the exit of the nozzle was calculated from the stagnation pressure, assuming isentropic flow between the helium pressure transducer and the nozzle exit. Likewise, the static pressure of the freestream air was computed from stagnation pressure measured in the settling chamber of the tunnel. The resulting operating conditions are listed in Table 1.

Experimental Apparatus and Techniques

Flow visualization was obtained by mercury arc lamp-based schlieren photography, a planar Rayleigh/Mie scattering technique, and acetone planar laser-induced fluorescence (PLIF). Velocity profiles were obtained with two-component LDV.

A Lambda Physik EMG 150 Excimer pulsed laser produced the 248-nm-wavelength uv radiation used for the Rayleigh/Mie scattering flow visualization. The laser beam was focused into a sheet and projected through the test section by a series of lenses and prisms. The sheet thickness was estimated to be 300 μm. Three separate configurations were used to obtain laser sheets in the $X-Y$, $X-Z$, and $Y-Z$ planes (Fig. 1). The Rayleigh/Mie scattering images were obtained by the scalar transport method.[21] The incident uv radiation was scattered off ice crystals formed from the moisture naturally present in the wind-tunnel supply air. The dry injected helium, on the other hand, was free of condensation particles. Thus, the Rayleigh/Mie images appear bright where air is present and dark where helium is present (with the exception of the recirculation zone; this will be discussed in the next section). Regions of mixed fluid fall between the bright and dark extremes. This visualization method using naturally present moisture has previously been used in supersonic boundary layers,[22] mixing layers,[15] and a transverse sonic jet.[23]

Whether the scattering is in the Rayleigh or Mie regime is not important so long as the particles accurately track the flow. Studies of condensation inside supersonic nozzles have shown that the ice crystals are nearly monodispersed with diameters between 0.003–0.014 μm, depending on the moisture content of the inlet air.[24] This size particle in the subject flowfield results in a Stokes number well below the upper limit of 0.5 calculated by Samimy and Lele[25] for acceptable particle size. Thus, as shown in previous investigations,[15,23] the ice crystals in the present flowfield are predicted to be small enough to accurately follow the large-scale turbulent fluctuations.

The scattered light signal was collected through a Nikon UV-Nikkor 105 mm f/4.5 telephoto lens and imaged onto the 578 × 384 pixel array of a Princeton Instrument Intensified charge-coupled device camera. The temporal duration of the laser pulse, approximately 20 ns, is sufficiently short to consider the images instantaneous.

Ensembles of 20 instantaneous images were recorded for selected locations and operating conditions. Both the streamwise (sheet in the $X-Y$ plane) and the spanwise (sheet in the $X-Z$ plane) images represent a 4.32 × 2.79 cm field of view (FOV), with the flow direction being left to right. The face-on images (sheet in the $Y-Z$ plane) represent a 3.05 × 2.03 cm FOV with the flow direction being out of the plane of the page. The camera was located approximately 30 deg off of the X axis for the face-on images. As a result, the original face-on images were compressed 8% in the spanwise Z direction. This image distortion was corrected during postprocessing. All of the instantaneous images presented in this article are representative of their respective ensembles.

Acetone PLIF images were acquired using uv radiation (266 nm) produced by a frequency-doubled Spectra-Physics Quanta-Ray DCR-4 Nd:YAG laser (λ = 532 nm) in conjunction with a Quanta-Ray wavelength extender (WEX-1). The amount of acetone added to the helium jet was regulated along with the helium gas flow rate. The same imaging system was used as in the Rayleigh/Mie setup, except that a Nikon Nikkor 60 mm f/2.8 Micro lens replaced the uv telephoto lens. Because acetone fluorescence is visible (λ = 350–600 nm), a standard camera lens can be used; an advantage of using a standard lens is that it effectively filters out the strong scattering from the particles in the flow and reflections from wind-tunnel wall surfaces at the wavelength of the incident radiation.

Results and Discussion

Base Flow Without Injection

The flowfield without injection was examined to establish a reference case against which the flowfield with helium injection from the various nozzle geometries could be evaluated. Figure 4 shows a schlieren photograph of the flowfield without

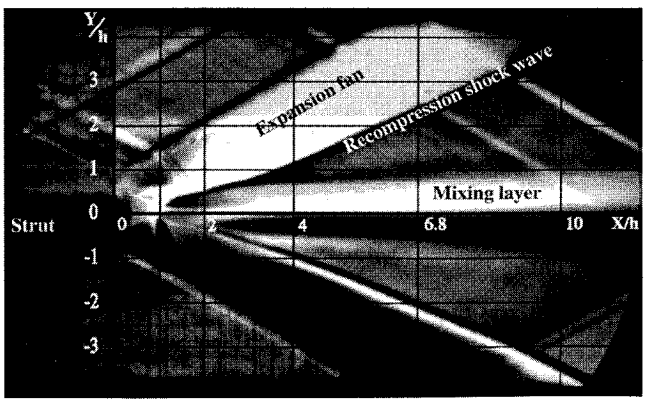

Fig. 4 Schlieren photograph of streamwise (X, Y) plane of view without injection.

injection. The flow is from left to right with $X/h = 0$ corresponding to the end of the strut. This image covers the 12.7 cm streamwise length of flow considered in this study. The vertical lines located at $X/h = 1, 2, 4, 6.8$, and 10 indicate the locations of the (X, Y) planes at which LDV data were collected and cross-sectional face-on views for the Rayleigh/Mie scattering images were recorded. These density gradients highlight the main features of the flowfield: expansion waves originating at the base of the strut, recompression shock waves, and mixing layers formed at the base of the strut between the primary flow and the recirculating flow. Since the time exposure of the schlieren photograph (1/400 s) is long compared to the time scale of motion of the flow, the density gradient effects are integrated over time as well as over the line of sight.

The LDV measurements acquired in the boundary layer on the surface of the strut ($X = -1.27$ cm) indicate a boundary-layer thickness of approximately $\delta = 5.6$ mm.[16] In addition, the boundary-layer turbulence intensities lie within the expected range for fully developed boundary layers when compared to data from previous studies.[16] As the incoming Mach 1.92 freestream flow expands over the edge of the base of the strut, a recirculation zone is created behind the base of the strut. The recirculation zone contains regions of both positive and negative streamwise velocities. Reverse mean streamwise velocities up to 8% of the freestream velocity were detected in the recirculation zone at $X/h = 1$. Because of a coarse measurement grid, a maximum reverse velocity was not obtained. The angle of the streamline at the boundary of the recirculation zone detected from the LDV data (18 deg) matches the angle visually approximated from Rayleigh/Mie scattering images. Two mixing layers, one on each side of the strut, are formed between the primary and recirculating flows. The location at which the two mixing layers merge is referred to as the recompression region. In this zone, the flow is compressed and two recompression shock waves are formed. The flowfield behind the base of the strut exhibits high-turbulence intensities in the recompression region (maximum measured intensity of 23%) and a drastic decrease in turbulence intensities downstream. The region occupied by the merged mixing layers is referred to as the wake of the strut. It is evident in Fig. 4 that the wake shows little spread in the transverse direction as it develops downstream.

Base Flow with Injection

Figure 5 shows the instantaneous Rayleigh/Mie images of the streamwise (X, Y) plane for the no-injection (N) case and the seven different helium injection cases ($\Psi = 4$) with the various nozzle configurations. The plane of view for these figures is located on the centerline of the tunnel with $X/h = 0$ corresponding to the end of the strut and the flow direction being from left to right.

The recirculation zone in the Rayleigh/Mie images appears as the dark triangular region behind the base of the strut in the flowfield without helium injection, as illustrated by the no-injection (N) case in Fig. 5. The static temperature of the recirculation zone is approximately equal to the stagnation temperature (300 K). This relatively high temperature drives the ice crystals formed in the freestream back into the vapor state, explaining the dark appearance of the recirculation zone in the Rayleigh/Mie image of the no-injection (N) case.

For the injection cases, the dark region at the base of the strut in the Rayleigh/Mie image is largely a result of the presence of helium (Fig. 5). However, as previously cited, the ice particles present in air captured in the recirculation zone are vaporized, thus the air in the recirculation zone also appears dark in the Rayleigh/Mie scattering images. Because of the similar appearance of air and helium in the recirculation zone, the Rayleigh/Mie scattering technique cannot be used to study the detailed evolution of the helium jet in the recirculation zone. This ambiguity is confined to the recirculation zone, since further downstream the evaporated water in the recirculating air condenses as it mixes with cold freestream air.

Acetone PLIF was used to visualize the helium jet structure in the recirculation zone, since the effectiveness of acetone fluorescence as a flow marker was not destroyed by the elevated temperature behind the base of the strut. Acetone was added to the helium reservoir that fed the jet flow. Figure 6 shows the resulting PLIF images for the helium jet injected from the circular (C) nozzle mounted in the base of the strut

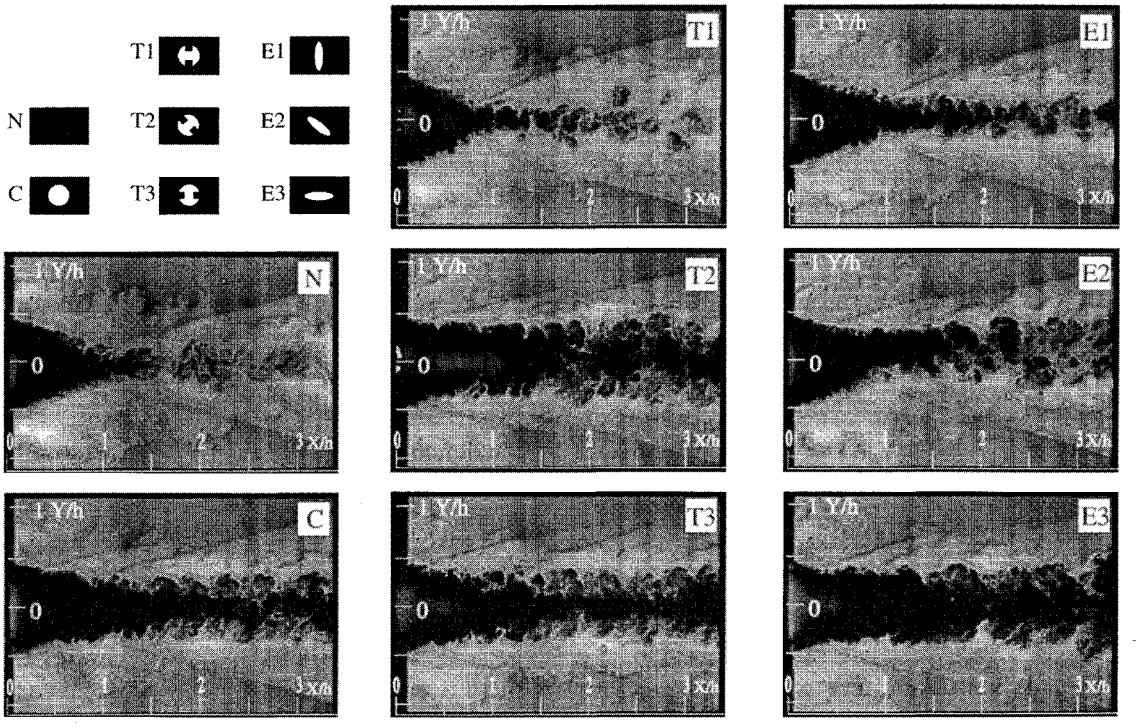

Fig. 5 Instantaneous Rayleigh/Mie images of streamwise (X, Y) plane of view located on the centerline of injector nozzle ($Z = 0$) for the no-injection (N) case and helium injection ($\Psi = 4$) cases (C, T1, T2, T3, E1, E2, and E3).

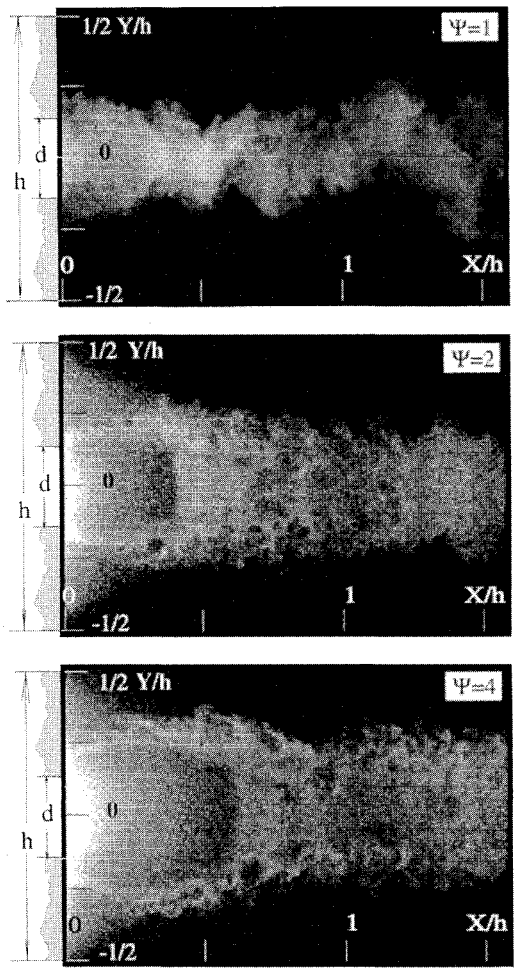

Fig. 6 Instantaneous acetone PLIF images of helium injection through circular nozzle (C) at static pressure ratios $\Psi = 1$, $\Psi = 2$, and $\Psi = 4$. Streamwise (X, Y) plane of view located on centerline of the jet ($Z = 0$).

into a Mach 1.92 freestream flow at jet-to-freestream static pressure ratios (Ψ) of 1, 2, and 4. Although the $\Psi = 4$ pressure ratio is the focus of this study, $\Psi = 1$ and 2 are shown here to demonstrate the effects of varying the static pressure ratio. The high-intensity (bright) regions show acetone fluorescence and reveal the presence of acetone vapor suspended in the helium jet. The images of the underexpanded jets ($\Psi = 2$, 4) show the presence of a barrel shock and a Mach disk. The Mach disks for $\Psi = 2$ and 4 appear to be located at about 5 and 8 mm downstream of the nozzle exit (i.e., $X/d_e = 1.4$ and 2.2, respectively). The acetone PLIF images show the presence of helium in the recirculation zone.

As the $\Psi = 4$ jet exits the nozzle at sonic speed, it expands within the bounds of the barrel shock to a calculated peak Mach number of about $M = 4$ before passing through the Mach disk[26] and becoming subsonic once again, after which the jet accelerates to a high subsonic or supersonic velocity as it mixes with the supersonic freestream air. The underexpanded jets show a higher initial jet radius, but the jets appear to be less undulating than the $\Psi = 1$ case. The $\Psi = 1$ jet also appears to be much more intermittent, suggesting the presence of large-scale structures.

Effect of Nozzle Geometry

To this point, the discussion of the flow visualization results has focused on the differences between the no-injection (N) and the baseline helium injection cases using the circular (C) nozzle. The following discussion focuses on the differences created by using different nozzle geometries for the helium injector.

For the injection cases, helium exits the nozzle into a low-velocity, low-pressure recirculation zone that approximates underexpanded freejet conditions. When the jet encounters the mixing layers formed between the primary freestream flow and the recirculating fluid at the base of the strut, it experiences azimuthal variation in pressure and velocity gradients, as well as turbulent mixing around its perimeter. This is unlike the axisymmetric gradients encountered at the circumference of a round free or coaxial jet. The mean streamwise velocity in the freestream adjacent to the top and bottom segments of the jet is higher than the velocity in the jet center, while the velocity in the wake flow on the spanwise sides of the jet is lower than the velocity in the jet center.[16] This creates a shear force on the top and bottom of the jet in the opposite direction to the shear force on the sides of the jet.

The recompression shock waves appear in the Rayleigh/Mie scattering images in the streamwise (X, Y) plane of view as the diverging dark lines in the freestream flow that diverge downstream (Fig. 5). The increase in pressure and corresponding increase in number density across the shock waves causes the flow to appear brighter downstream of the shock waves. Evidently, the increase in temperature across the shock waves is not enough to sublimate the ice particles and to counteract the increase in number density because of the pressure rise. For the no-injection (N) case, a two-dimensional recompression shock wave is generated at the location where the mixing layers merge.

When helium is injected from the base of the strut, additional shock waves appear upstream of the nominally two-dimensional recompression shock waves. They result from the intersection of the mixing layers and the helium jet. Given that the injector nozzle exit is circular or elliptic, it is not surprising that the shock waves formed by the interaction of the jet with the nominally two-dimensional mixing layers are three dimensional. In fact, they appear very much like longitudinal segments of a cone. For this reason and for the sake of clarity, these initial shock waves resulting from the jet/mixing layer interaction will be referred to as conical shock waves.

Figure 7 shows the instantaneous Rayleigh/Mie image of the face-on plane of view located at $X/h = 1$. The flow direction is out of the page. The dark region in the center of the image represents the helium jet and the dark strip across the image represents fluid from the recirculation zone. The conical shock waves appear as the arcs above and below the strut, enclosing a bright region. They are most pronounced (largest curvature) for the T3 and E3 cases and barely noticeable for the T1 and E1 cases. The strength of the conical shock wave indicates the extent to which the jet spreads in the transverse direction and disturbs the nominally two-dimensional mixing layers.

The instantaneous Rayleigh/Mie images of the face-on plane of view at $X/h = 2$ are shown in Fig. 8. Comparison of the results in Figs. 7 and 8 show the development of large-scale structures in the flow as well as the nominally two-dimensional recompression shock and the conical shock waves. The series of weak nominally two-dimensional shock waves appear as series of horizontal dark lines spanning the image slightly above and below the jet in Fig. 8; these waves coalesce to form a single stronger recompression shock wave. The bright region sandwiching the jet is a consequence of the primary flow having experienced a pressure increase (and corresponding number density increase) as it passed through the nominally two-dimensional recompression shock waves. This intensity increase was also evident in the streamwise images (Fig. 5). The instantaneous images show an array of structures of different sizes at the interface between the jet and the primary flow. Figure 9 shows the average Rayleigh/Mie image of the face-on plane of view at $X/h = 2$. The average images exemplify the large-scale stationary structures since the nonstation-

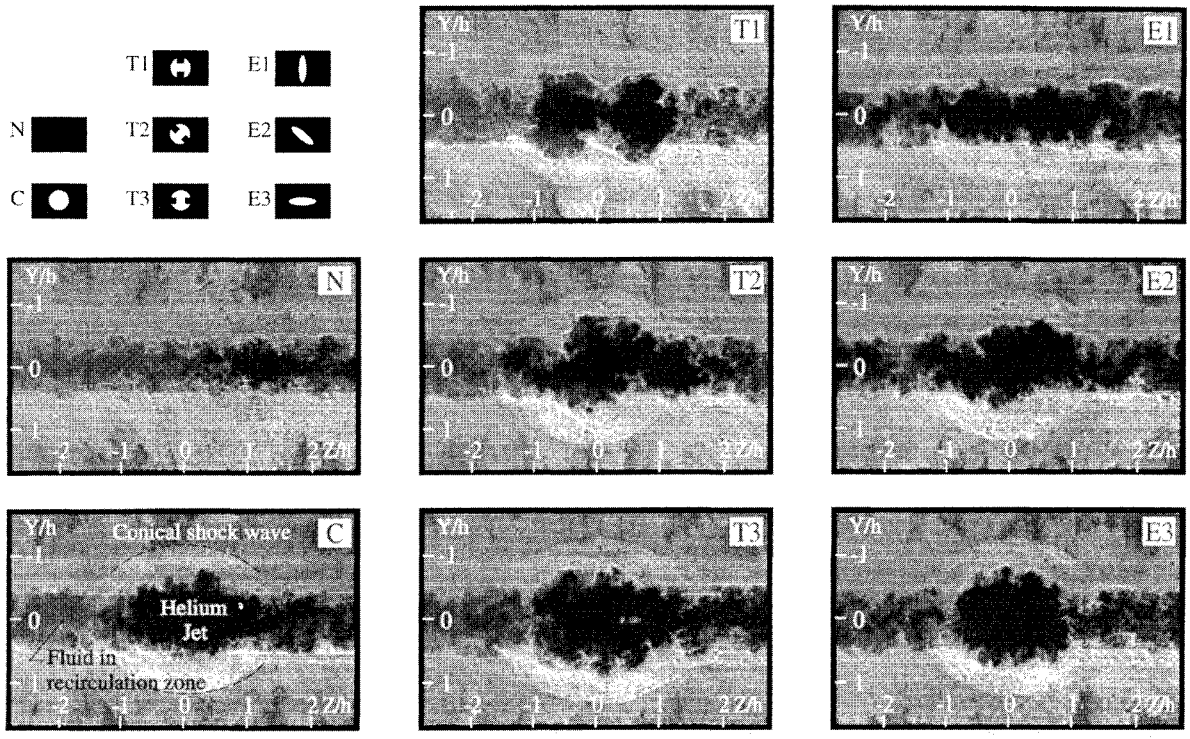

Fig. 7 Instantaneous Rayleigh/Mie images of face-on (Y, Z) plane of view located at X/h = 1 for the no-injection (N) case and helium injection (Ψ = 4) cases (C, T1, T2, T3, E1, E2, and E3).

ary structures are filtered-out in the image averaging process. The face-on images show the jet shape most clearly as it develops downstream. The jet shapes created by each nozzle are distinctly different for the face-on images at X/h = 1, 2, and 4 (Figs. 7–10), but lose their form as they travel further downstream to the point that they are nondescript at X/h = 10.[16]

Since the air in the recirculation zone behind the strut is of relatively low velocity and at a lower pressure as compared to the helium at the injector nozzle exit, the injected jet is expected to behave much like an underexpanded free jet until it interacts with the mixing layers formed between the primary flow and the recirculating flow at the base of the strut. It is obvious from the face-on images of the jet in Figs. 7–10 that the mixing layers formed between the primary and recirculating flows severely restrict jet spread in the transverse direction. This is most evident for the C, T3, and E3 cases as discussed in the following paragraphs.

Circular Nozzle Configuration (C)

For helium injection from the circular (C) nozzle, an oblong jet is produced, whereas a circular jet would be expected in the freejet case (Fig. 9). Using terminology for an ellipse, the major-axis of the oblong jet cross section is a little over twice the minor-axis dimension at X/h = 2. The structures seen at the circumference of the jet in the instantaneous images are averaged out, for the most part, on the average images of the circular (C) nozzle except for the lobe protruding from the upper right corner of the jet cross section on the images at X/h = 1, 2, and 4 (Figs. 7–10). The fact that the lobe appears on the average images indicates that it is spatially stationary and propagates downstream without significant changes until X/h > 4. This anomaly in the jet shape is likely a result of a perturbation that is enhanced by Taylor–Gôrtler type instability, inherent in underexpanded jets, which creates a pair of counter-rotating vortices with the sense of rotation to eject jet fluid into the primary flow.[27] The source of perturbation could be as minute as a scratch inside the nozzle.[28] By X/h = 6.8 m (Fig. 11), the well-defined large-scale structures have disappeared and the jet achieves a more circular cross section on average, and by X/h = 10 only a small amount of core fluid is left unmixed.[16]

Circular-with-Tabs Nozzle Configurations (T1, T2, and T3)

Previous studies have shown that tabs in subsonic and supersonic freejets generate a pair of counter-rotating vortices that engulf ambient fluid.[7,8,17] The generation of these vortices has been attributed to a pressure hill upstream of the tab and a lower pressure downstream of the tab. The strength of the pressure gradient was seen to increase with an increase in jet-to-freestream pressure ratio.[17] As a result, one would expect that the circular-with-tabs nozzle cases (T1, T2, and T3) would generate counter-rotating vortices like those sketched in Fig. 12.

Indeed, it does appear that these vortices are initiated at the exit of the circular-with-tab nozzles. The mixing layers formed between the primary and recirculating flows at the base of the strut appear to either reinforce or suppress these vortices depending on the orientation of the nozzle with respect to the base flow. The interaction between the mixing layers and the counter-rotating vortices in the jet can be understood by considering the freejet dynamics for injection from a circular nozzle with two tabs, combined with the dynamics of the flow around the base of the strut without injection. For a freejet emanating from a circular (C) nozzle with two tabs, the jet fluid is expected to flow predominantly in the streamwise direction along the axis of the nozzle. However, a strong secondary flow is present in the direction radially outward along a line perpendicular to a line connecting the two tabs.[8] The expected flow directions and vortices generated by each tab are shown in Fig. 12. For the T1 case, this motion is directed along the spanwise axis of the tunnel, tangent to the mixing layers. This same secondary motion of jet fluid for the T2 case is directed at a 45-deg angle into the mixing layers on the top and bottom of the strut. For the T3 case, the motion is directly into the mixing layers, i.e., normal to the mixing layers.

The presence of the mixing layers in the T1 case appears to reinforce the effect of the counter-rotating vortices at each tab to engulf freestream air and quickly bifurcate the jet into two

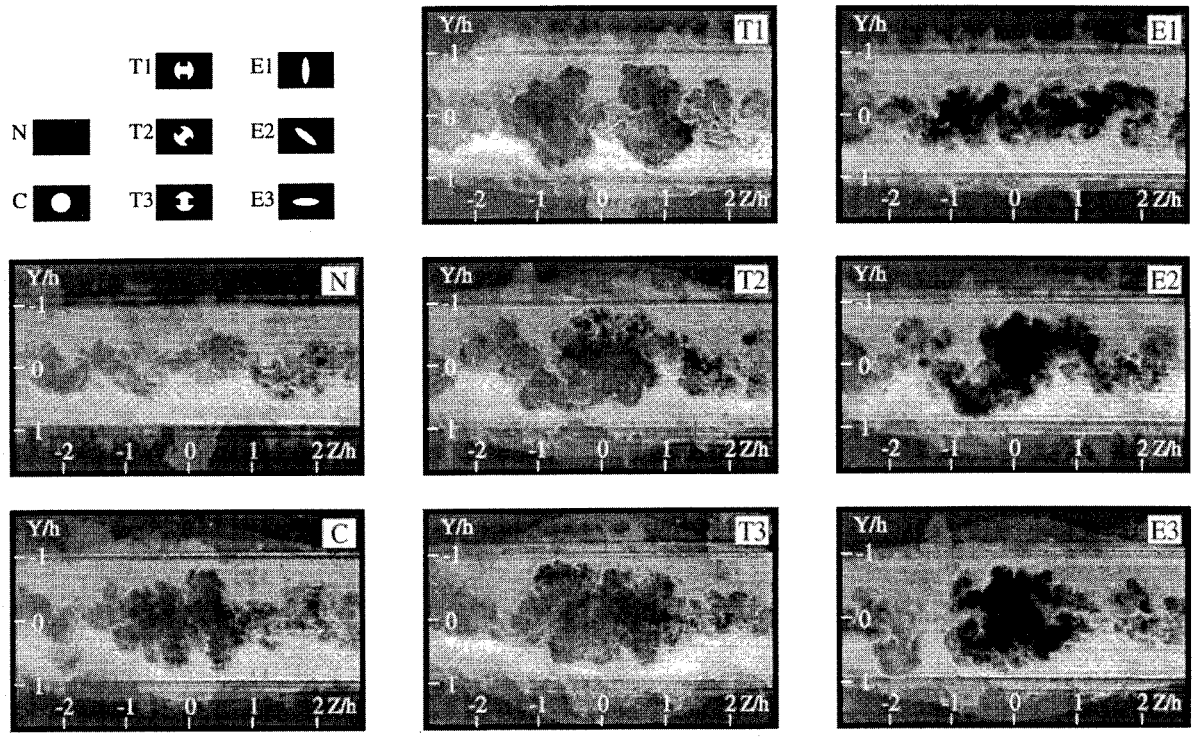

Fig. 8 Instantaneous Rayleigh/Mie images of face-on (Y, Z) plane of view located at X/h = 2 for the no-injection (N) case and helium injection (Ψ = 4) cases (C, T1, T2, T3, E1, E2, and E3).

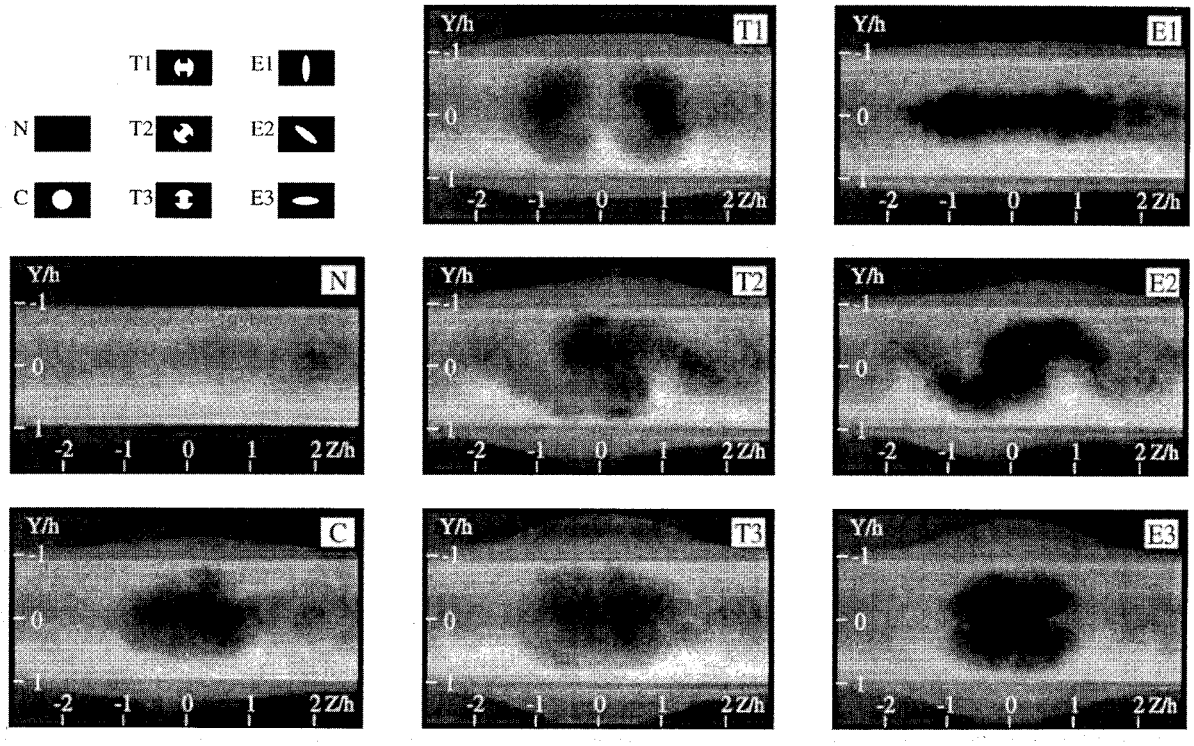

Fig. 9 Average Rayleigh/Mie images of face-on (Y, Z) plane of view located at X/h = 2 for the no-injection (N) case and helium injection (Ψ = 4) cases (C, T1, T2, T3, E1, E2, and E3).

adjacent cores. Bifurcation in the T1 case is clearly evident in the face-on views at X/h = 1, 2, and 4 (Figs. 7–10). The bifurcation is so pronounced that it appears, on the streamwise (X, Y) plane Rayleigh/Mie images, almost as if there were no jet on the centerline, i.e., the T1 case looks nearly identical to the no-injection (N) case (Fig. 5). The plan (X, Z) view Rayleigh/Mie images show that the two core centers become distinct at approximately X/h = 1 and travel in nearly parallel paths downstream.[16]

For the T2 case, it is evident that the pair of streamwise vortices created by the tabs is distorted by the mixing layer to form the S like jet contour shown in the end views of Fig. 8. Since the strength of the conical shock depends on the degree of the interaction between the jet and the mixing layers, the conical shock wave can be used to identify where the most significant jet–wake flow impingement occurs around the jet perimeter, and the relative strengths of the interactions. The conical shock for the T2 case is asymmetric (Fig. 7) with the

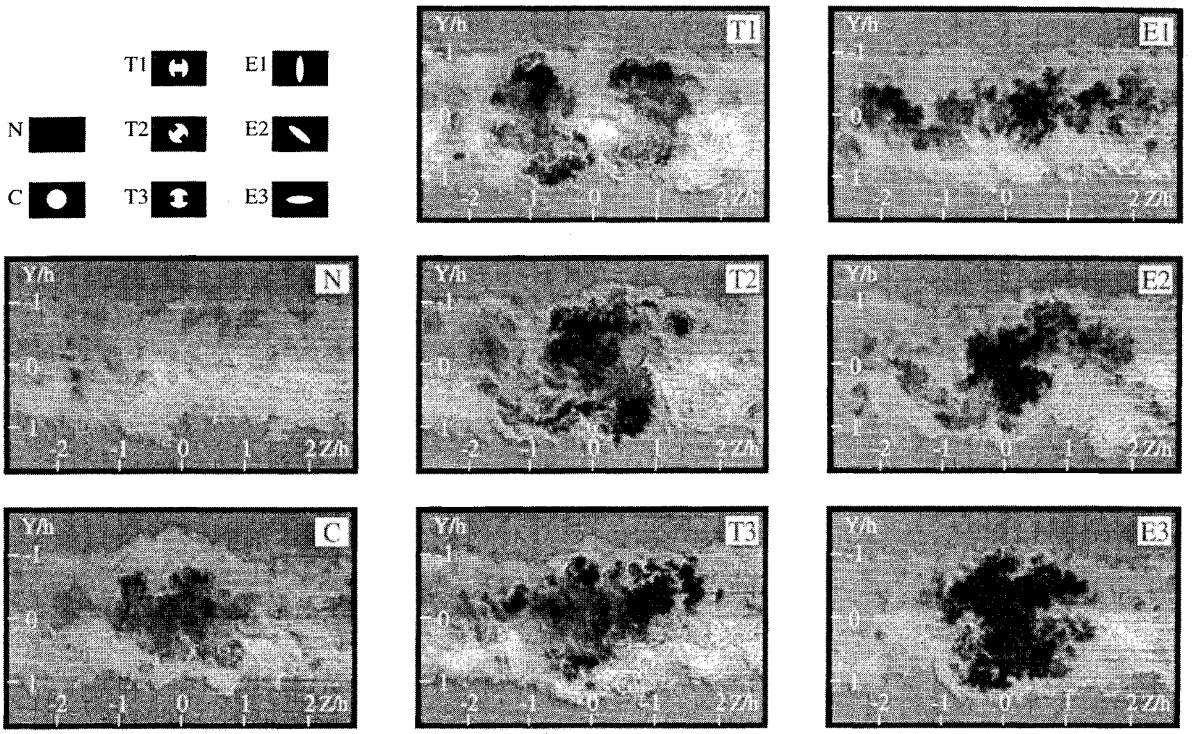

Fig. 10 Instantaneous Rayleigh/Mie images of face-on (Y, Z) plane of view located at X/h = 4 for the no-injection (N) case and helium injection (Y = 4) cases (C, T1, T2, T3, E1, E2, and E3).

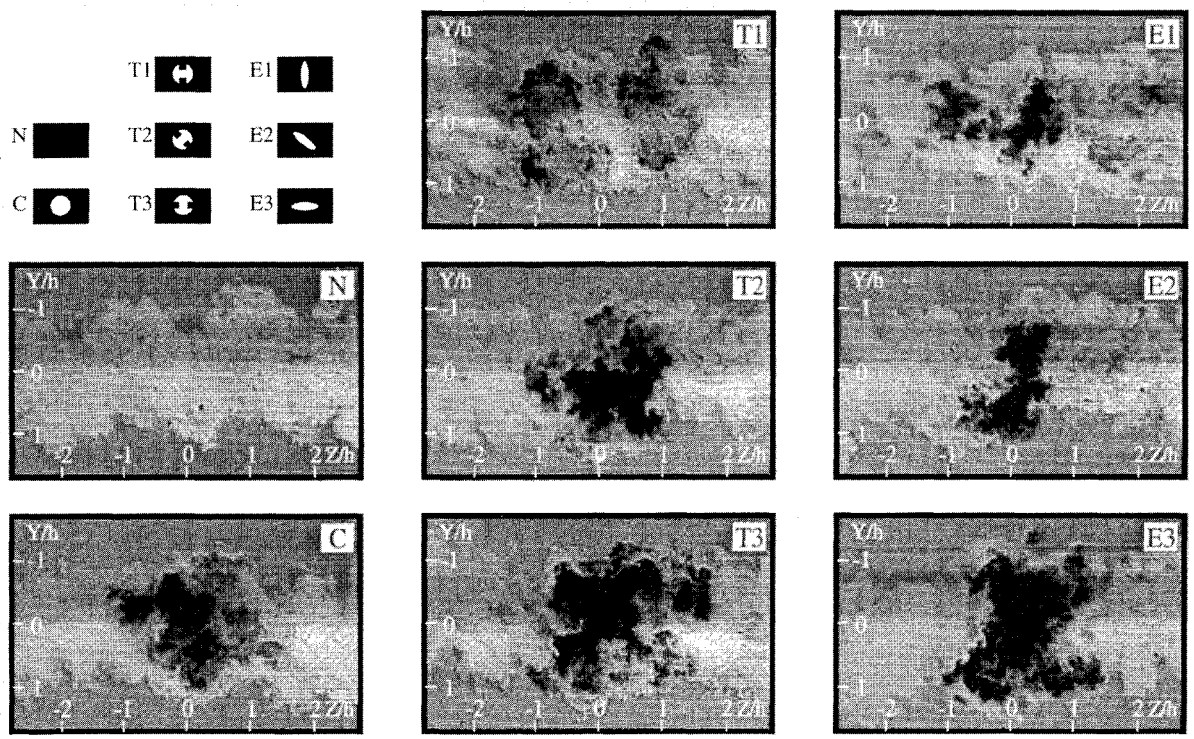

Fig. 11 Instantaneous Rayleigh/Mie images of face-on (Y, Z) plane of view located at X/h = 6.8 for the no-injection (N) case and helium injection (Y = 4) cases (C, T1, T2, T3, E1, E2, and E3).

strongest interaction (largest curvature) being at the location of the largest secondary, radial motion of the jet. Bright wisps of freestream fluid penetrating the T2 jet region and appearing on the instantaneous and average images at X/h = 1 and 2 (Figs. 7–9) show that primary flow is engulfed in the same orientation as the tab locations. This is presumably a result of the counter-rotating pair of streamwise vortices generated by each tab.

A noticeably larger conical shock wave is generated for the T3 case since the strongest radial component of jet flow generated by the tabs in this orientation was expected to be directly toward, i.e., normal to the mixing layers rather than at an angle to them as in the T2 case or tangent to them as in the T1 case. The two-dimensional mixing layers appear to have drastically suppressed the action of the vortices generated by the tabs in the T3 case (Figs. 7–10). Concrete evidence of

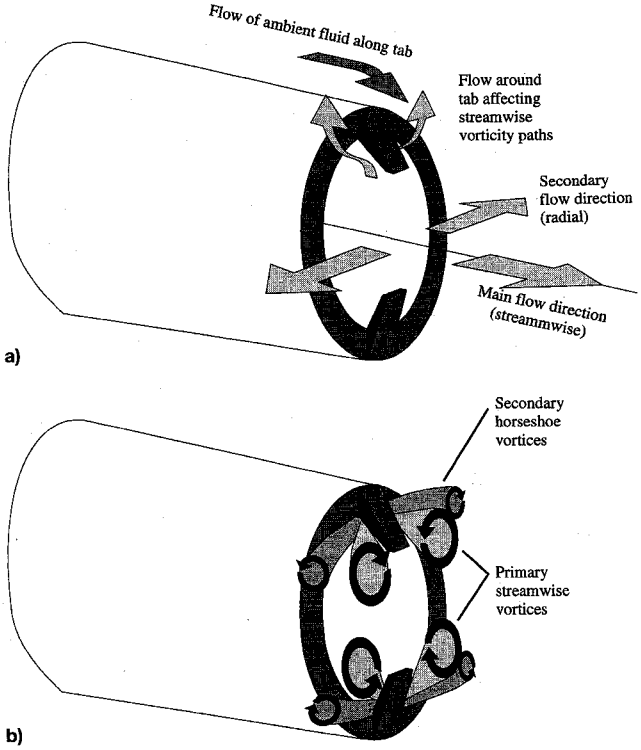

Fig. 12 Illustration of a) primary counter-rotation vortices and secondary horseshoe vortices for flow around a delta tab at a 135-deg angle to the nozzle wall and b) primary and secondary flow patterns of fluid emanating from a circular nozzle with two delta tabs at 135 deg to the nozzle wall.

stationary streamwise vortices is not seen in the face-on Rayleigh/Mie images until $X/h = 6.8$ where it appears that the primary fluid is ingested at the sides of the jet as indicated by the indents in the jet (Fig. 11). This is evidence of the presence of counter-rotating vortices at the downstream locations. Note that the total pressure losses from forcing the flow around the tabs could be considerable.[17] Thus, there is a tradeoff between increasing the mixing and preserving the fuel's total pressure for increasing engine thrust.

Elliptic-Nozzle Configurations (E1, E2, and E3)

Jets emanating from elliptic nozzles evolve differently from those emanating from circular (and circular-with-tabs) nozzles. The elliptic jets begin with different dynamics. The large azimuthal variation in curvature of the elliptic vortical structures causes nonuniform self-induction and subsequent complex three-dimensional deformation. The most notable phenomenon of an oblong jet is axis-switching, in which the jet cross section contracts in the direction of the major-axis and expands along the minor-axis, so that the two axes are eventually interchanged.[19] This phenomenon is believed to be intimately related to the nonuniform momentum thickness distribution around the jet perimeter.[29]

It is evident from the Rayleigh/Mie scattering images that motion of the jet fluid emanating from the elliptic-nozzle configurations (E1, E2, and E3) is modified by the mixing layers when compared to jets emanating from elliptic nozzles in a freejet situation. This is most obvious when comparing the evolution of the jets emanating from the E1 and E3 nozzles. The jet emanating from the E1 nozzle configuration appears to have switched axes immediately upon exiting the nozzle while the jet emanating from the E3 configuration appears to switch axes much further downstream (Figs. 7–10). It appears from Fig. 7 that the elliptic jet in the E1 orientation has gone through one-axis-switch by $X/h = 1$ and has achieved an AR greater than three by $X/h = 4$ (Fig. 10). Face-on images further downstream show that the E1 jet continues to spread along its new major-axis and does not incur another axis-switching. The mixing layers do not appear to hinder the observed axis-switching in the E1 case and, perhaps, even induced the axis-switch and subsequent jet spread in the spanwise direction. On the other hand, the jet emanating from the E3 nozzle remains rather compact until $X/h = 6.8$ where it then elongates slightly in the transverse direction to achieve one axis-switch (Fig. 11). Noticeable curls are present on the sides of the jet in the instantaneous face-on Rayleigh/Mie images at $X/h = 2$, 4, and 6.8 (Figs. 8–11). These curls are presumably caused by streamwise vortices. They appear to be spatially stationary, judging from the indents in the sides of the jet in the average image in Fig. 9. These indents indicate the presence of engulfed air between the location of the curls seen in the average images at $X/h = 2$, 4, and 6.8. The AR of the E3 jet at $X/h = 6.8$ is approximately half that of the E1 jet at $X/h = 4$, showing that the mixing layers suppress the E3 jet dynamics relative to the E1 jet.

The instantaneous and average plan view images of the E1 jet[16] show that the jet core bifurcated, albeit less completely than in the T1 case, and that each core appears to be traveling away from the centerline as opposed to the T1 case, in which the separated cores travel along relatively parallel paths. Bifurcation of a subsonic freejet emanating from an elliptic nozzle is explained by a connecting type action of adjacent sides of the elliptic vortical ring structure.[19] If the connection becomes complete, the elliptic jet appears pinched and separated into two adjacent, almost circular, jets. A distorted axis-switch is seen for the E2 case. The ends of the major axis of the elliptic E2 jet were distorted by the wake flow in a manner similar to the T2 case and also formed an S-shaped jet cross-sectional area (Fig. 9).

The transition between mixing dominated by large-scale effects near the base of the strut and mixing dominated by small-scale effects further downstream is suggested by several factors. First, the significant variation in velocity at $X/h = 2$ becomes uniform by $X/h = 6.8$, signifying that the bulk of the mixing occurs upstream of $X/h = 6.8$.[16] Second, the centerline velocity distribution for the circular (C) case shows a transition point somewhere between $X/h = 6$ and 7, signifying a decrease in mixing activity.[16] Similarly, a large structure appearing as a lobe on the circular (C) jet in the average face-on view Rayleigh/Mie scattering images at $X/h = 1$, 2, and 4 is not apparent at $X/h = 6.8$, signifying that the large-scale structures diminish by $X/h = 6.8$.

The standard deviation of the ensemble of face-on images at $X/h = 10$ show the smallest fluctuations for T1 and E1.[16] Since this is in the region of diminishing structure size this suggests that the T1 and E1 cases are the most completely mixed by $X/h = 10$. This supports the observation from the instantaneous and mean images that the T1 and E1 cases appear most thoroughly mixed by the last measurement location at $X/h = 10$.[16]

Conclusions

The flowfield without injection was examined to establish a reference case against which the flowfield with helium injection from the various nozzle geometries could be evaluated. LDV measurements show the incoming boundary layer to be fully developed and the freestream flow to be uniform and symmetric above and below the strut with a calculated Mach number of 1.92 and turbulence intensity values of less than 1%. The boundary-layer thickness δ was determined to be 5.6 mm with a peak streamwise turbulence intensity of about 7%. The predicted angles of the leading and trailing expansion waves, emanating from the top and bottom shoulders of the base, using the Prandtl–Meyer theory, match the angles apparent on the schlieren photograph.

The mixing interaction between the jet and the primary flow occurs within the confines of the region marked by the wake behind the strut. Thus, the jets exhibit limited spread in the

transverse (Y) direction, which limits mixing with the primary freestream flow.

The various nozzle geometries create different dynamics that affect the overall mixing of the injectant with the primary air. The axis-switching phenomenon apparent in freejets issued from oblong nozzle geometries is apparent for the jets issuing from the elliptic nozzles in this study. However, interaction of the mixing layers with the jet appears to accelerate an axis switch in the E1 case, distort the axis switch in the E2 case, and hinder the axis switch in the E3 case. The effect of the mixing layer on axis switching can be understood by considering an oblong freejet where the asymmetric development of vorticity around the perimeter is believed to be primarily responsible for axis-switching. Likewise, bifurcation similar to that occurring in freejets issuing from a nozzle with two tabs is clearly seen in the case of the circular-with-tabs nozzle in this study with the T1 orientation. The effect of the mixing layers on the bifurcation of the jet can be understood by considering the development of the pair of counter-rotating streamwise vortices generated by each tab that engulf surrounding fluid, and by considering the ejection of jet fluid into the surrounding fluid by the radial component of velocity perpendicular to the nozzle diameter connecting the two tabs. The orientation of the nozzle relative to the mixing layers dictates whether the mixing layers reinforce or suppress jet development.

Visual inspection of the instantaneous and average Rayleigh/Mie scattering images, particularly those of the face-on (Y, Z) plane of view, suggests that the T1 jet mixes most effectively, followed by the E1 case with the T3, T2, and C cases incurring the least effective mixing. In agreement with the LDV streamwise velocity profiles, the Rayleigh/Mie images show the E1 case to spread the most in the spanwise (Z) direction but the E1 jet remains more coherent than the T1 case.

Acknowledgments

This work was supported by the Palace Knight Program and by the Aero Propulsion and Power Directorate of the Wright Laboratory under Contract F33615-93-C-2300. The authors are indebted to C. Carter and M. Gruber for helpful discussions; and D. Schommer, C. Smith, K. Kirkendall, and G. Haines for technical assistance; A. Creese and S. Arnette for technical editing; and to J. Solari for graphic layout.

References

[1]Heppenheimer, T. A., "Keepers of the Flame," *Air & Space*, Jan. 1990, pp. 88–95.

[2]Papamoschou, D., and Roshko, A., "The Compressible Turbulent Shear Layer: An Experimental Study," *Journal of Fluid Mechanics*, Vol. 197, Dec. 1988, pp. 453–477.

[3]Samimy, M., and Elliott, G. S., "Effects of Compressibility on the Characteristics of Free Shear Layers," *AIAA Journal*, Vol. 28, No. 3, 1990, pp. 439–445.

[4]King, P. S., Thomas, R. H., Schetz, J. A., and Billig, F. S., "Combined Tangential-Normal Injection into a Supersonic Flow," AIAA Paper 89-0622, Jan. 1989.

[5]McClinton, C. R., "The Effect of Injection Angle on the Interaction Between Sonic Secondary Jets and a Supersonic Free Stream," NASA TN D-6669, Feb. 1972.

[6]Gutmark, E., Schadow, K. C., and Wilson, K. J., "Subsonic and Supersonic Combustion Using Noncircular Injectors," *Journal of Propulsion and Power*, Vol. 7, No. 2, 1991, pp. 240–249.

[7]Samimy, M., Zaman, K. B. M. Q., and Reeder, M. F., "Effect of Tabs on the Flow and Noise Field of an Axisymmetric Jet," *AIAA Journal*, Vol. 31, No. 4, 1993, pp. 609–619.

[8]Reeder, M. F., and Samimy, M., "The Evolution of a Jet with Vortex Generating Tabs: Real-Time Visualization of Quantitative Measurements," *Journal of Fluid Mechanics*, Vol. 311, March 1996, pp. 73–118.

[9]Jacobs, J. W., "Shock Induced Mixing of a Light-Gas Cylinder," *Journal of Fluid Mechanics*, Vol. 132, 1992, pp. 319–336.

[10]Waitz, I. A., Marble, F. E., and Zukoski, E. E., "Vorticity Generation by Contoured Wall Injectors," AIAA Paper 92-3550, July 1992.

[11]Samimy, M., and Addy, A. L., "Interaction Between Two Compressible Turbulent Free Shear Layers," *AIAA Journal*, Vol. 24, No. 12, 1986, pp. 1918–1923.

[12]Amatucci, V. A., Dutton, J. C., Kuntz, D. W., and Addy, A. L., "Two-Stream Supersonic Wake Flow Field Behind a Thick Base, Part I: General Features," *AIAA Journal*, Vol. 30, No. 8, 1992, pp. 2039–2046.

[13]Dutton, J. C., Herrin, J. L., Molezzi, M. J., Mathur, T., and Smith, K. M., "Recent Progress on High-Speed Separated Base Flows," AIAA Paper 95-0472, Jan. 1995.

[14]Gruber, M. R., and Nejad, A. S., "New Supersonic Combustion Research Facility," *Journal of Propulsion and Power*, Vol. 11, No. 5, 1995, pp. 1080–1083.

[15]Elliott, G. S., Samimy, M., and Arnette, S. A., "A Study of Compressible Mixing Layers Using Filtered Rayleigh Scattering," *AIAA Journal*, Vol. 30, No. 10, 1992, pp. 2567–2569.

[16]Glawe, D. D., "The Effects of Nozzle Geometry on Injection from the Base of a Strut into Supersonic Flow," Ph.D. Dissertation, Ohio State Univ., Columbus, OH, 1995.

[17]Zaman, K. B. M. Q., Reeder, M. F., and Samimy, M., "Control of an Axisymmetric Jet Using Vortex Generators," *Physics of Fluids*, Vol. 6, No. 2, 1994, pp. 778–793.

[18]Schadow, K. C., Wilson, K. J., Lee, M. J., and Gutmark, E., "Enhancement of Mixing in Reacting Fuel-Rich Plumes Issued from Elliptical Nozzles," *Journal of Propulsion and Power*, Vol. 3, No. 2, 1987, pp. 145–149.

[19]Hussain, F., and Husain, H. S., "Elliptic Jets. Part I. Characteristics of Unexcited and Excited Jets," *Journal of Fluid Mechanics*, Vol. 208, Nov. 1989, pp. 257–320.

[20]Haimovitch, Y., Gartenberg, E., Roberts, S. A., Jr., and Northam, G. B., "An Investigation of Wall Injectors for Supersonic Mixing Enhancement," AIAA Paper 94-2940, June 1994.

[21]Clemens, N. T., and Mungal, M. G., "A Planar Mie Scattering Technique for Visualizing Supersonic Mixing Flows," *Experiments in Fluids*, Vol. 11, Nos. 2, 3, 1991, pp. 175–185.

[22]Arnette, S. A., Samimy, M., and Elliott, G. S., "Structure of a Supersonic Boundary Layer After Various Regions of Expansion," *AIAA Journal*, Vol. 33, No. 3, 1995, pp. 430–438.

[23]Gruber, M. R., Nejad, A. S., Chen, T. H., and Dutton, J. C., "Mixing and Penetration Studies of Sonic Jets in a Mach 2 Freestream," *Journal of Propulsion and Power*, Vol. 11, No. 2, 1995, pp. 315–323.

[24]Wegener, P. P., and Parlange, J. Y., "Non-Equilibrium Nozzle Flow with Condensation," *AGARD Recent Advances in Aerothermochemistry* (Oslo, Norway), 1967, pp. 607–634.

[25]Samimy, M., and Lele, S. K., "Motion of Particles with Inertia in a Compressible Free Shear Layer," *Physics of Fluids A*, Vol. 3, No. 8, 1991, pp. 1915–1923.

[26]Chen, M. H., Gaffney, R., Wu, P. K., and Nejad, A. S., "Numerical Simulations of Axisymmetric Sonic He and H_2 Injections into a Mach 2 Airstream," AIAA Paper 95-0873, Jan. 1995.

[27]Arnette, S. A., Samimy, M., and Elliott, G. S., "On Streamwise Vortices in High Reynolds Number Supersonic Axisymmetric Jets," *Physics of Fluids A*, Vol. 5, No. 1, 1993, pp. 187–202.

[28]Novopashin, S. A., and Perepelkin, A. L., "Axial Symmetry Loss of a Supersonic Preturbulent Jet," *Physics Letters A*, Vol. 135, Nos. 4, 5, 1989, pp. 290–293.

[29]Koshigoe, S., Gutmark, E., Shadow, K. C., and Tubis, A., "Initial Development of Noncircular Jets Leading to Axis Switching," *AIAA Journal*, Vol. 27, No. 4, 1989, pp. 411–419.